



Karstic aquifer structure from geoelectrical modeling in the Ring of Sinkholes, Mexico

Luisa Andrade-Gómez¹ · Mario Rebolledo-Vieyra^{2,3} · José Luis Andrade¹ · Paloma Z. López^{2,4} · José Estrada-Contreras^{2,3}

Received: 29 June 2018 / Accepted: 6 July 2019 / Published online: 31 July 2019
© Springer-Verlag GmbH Germany, part of Springer Nature 2019

Abstract

Groundwater models based on terrain resistivity can show the diverse properties and processes occurring between fractures, boreholes and conduits. Using electrical resistivity tomography, a conceptual model was created of the aquifer within the Ring of Cenotes, which surrounds the Chicxulub Crater on the Yucatan Peninsula, Mexico. Determining the hydrogeological parameters of an aquifer is vital since they determine flux and hydrodynamic patterns. In karstic environments, conventional techniques are not effective at recording heterogeneities such as fracture zones and conduits. Six transects were investigated among areas near cenotes (sinkholes) and *aguadas* (small surface-water bodies), as well as areas lacking these formations. The resulting profiles reached up to 30 m deep and showed an aquifer consisting of a fractured matrix saturated with freshwater. The matrix exhibiting resistivity values from 3 to 250 Ωm , lying under a vadose zone with values from 300 to 25,000 Ωm . *Aguadas* and cenotes are surface manifestations of the aquifer's internal structure, which is a network of caves and conduits. In the Ring of Cenotes, the presence of these surface formations indicates increased hydraulic conductivity in their vicinity, with smaller conduits or fractures providing lesser conductivity in areas further away.

Keywords Karst · Coastal aquifer · Hydrogeology · Geophysical methods · Yucatan, Mexico

Introduction

Karstic formations are highly heterogeneous systems consisting of a porous matrix surrounding fractures and conduits (Fairchild and Baker 2012). The carbonate matrix provides subterranean water drainage as does an associated system of integrated faults, conduits and broadly dilated or poorly modified fractures (Toran et al. 2007). These structural characteristics define a system's

hydrodynamic responses, local and regional connectivity, pollutant dispersion and water availability.

The northern Yucatan Peninsula (YP) in Mexico is considered a coastal karstic aquifer. On its surface, different hydrological formations are found with unique characteristics and ecosystems. A hydrogeological structure running around the Chicxulub Crater, a ring of sinkholes, locally known as “Ring of Cenotes” (RC), occupies the northern region of the Peninsula (Rebolledo-Vieyra et al. 2011). The RC differs from the rest of the aquifer in that it has higher hydraulic conductivity than surrounding areas and poor storage capacity (Null et al. 2014), as well as a marked seasonal response (Marín 1990). The RC is a high concentration of cenotes formed by the roof collapse of tall dissolution features (Pope et al. 1996), and other bodies of water called *aguadas*. The water level response to seasonal changes, within cenotes and *aguadas*, is determined by the surrounding matrix. The water present in *aguadas* has long been believed to be directly surface water from seasonal precipitation and, therefore, not connected to the aquifer (Finch 1965). In contrast, cenotes always contain water, and are connected to the aquifer and other cenotes through fractures and conduits (Schmitter-Soto et al. 2002). Cenotes have a high probability of local-scale connection (Gómez-Nicolás et al.

✉ Mario Rebolledo-Vieyra
mariormx@gmail.com

¹ Unidad de Recursos Naturales, Centro de Investigación Científica de Yucatán, A.C, Calle 43 No. 130, Col. Chuburna de Hidalgo, 97200 Mérida, Yucatán, Mexico
² Unidad de Ciencias del Agua, Centro de Investigación Científica de Yucatán, A.C, Calle 8 No. 39, Mz. 29, S.M. 64, 77500 Cancún, Quintana Roo, Mexico
³ Present address: Chipre No. 5, Resid. Isla Azul, Cancún, Quintana Roo, Mexico
⁴ Present address: Bermuda Institute of Ocean Sciences, 17 Biological Station, Ferry Reach, St. George's GE 01, Bermuda

2017), and chemical composition can be similar among various cenotes in some regions of the RC (Pérez-Ceballos et al. 2012). Both aguadas and cenotes support extensive socio-economic and environmental networks, and the local human populations which depend on them have a growing interest because of the water and food security they provide.

Extensive previous research on the RC has employed conventional techniques such as hydrochemistry, geophysics (seismic refraction (Gulick et al. 2008) and magnetotellurics (Delgado-Rodríguez et al. 2001)) and exploratory SCUBA diving (Bauer-Gottwein et al. 2011; Ford and Williams 2013). These have helped to define areas or groups of cenotes (e.g. Pérez-Ceballos et al. 2012), establish flow patterns (e.g. Perry et al. 2002; Steinich and Marin 1996; Steinich and Marín 1997), and define resources (e.g. La Reserva Geohidrológica del Anillo de Cenotes; Decree 117 2018); all have contributed to use and management decision making. The limitations of conventional techniques have precluded an understanding of system spatial heterogeneity, causing serious challenges in developing regional models (Vuilleumier et al. 2013), local and regional connectivity studies (Gómez-Nicolás et al. 2017), and resource estimation and management studies.

Electrical resistivity tomography (ERT) has been widely used to characterize the geological structure of aquifers and their surroundings (Bechtel et al. 2007; Griffiths and Barker 1993). Its application has contributed to solving regional and local geological problems linked to system geology, geological structure or the presence of hydro-stratigraphic sequences (Loke et al. 2013). The physical property of materials such as resistivity, recorded in ERT images, allow construction of the conceptual models required for development of mathematical models (Anderson and Woessner 1992).

The present study objective is to characterize the shallow structure of a karst aquifer based on resistivity profiles. Because of the high regional hydraulic conductivity in the RC, the high cenote density, the fractures surrounding the crater (Gulick et al. 2008; Rebolledo-Vieyra et al. 2010) and the permeability variation, correlated with facies change (Fitchen et al. 1995; Rebolledo-Vieyra et al. 2000), it is hypothesized here that the aquifer is contained in a limestone matrix with greater local conductivity associated with the presence of these structures. This paper characterizes the distribution of apparent resistivity using ERT sections. These are presented and interpreted to constrain hydrogeological models from areas above and between cenotes and aguadas, as well as at locations far from these formations. A conceptual regional model is proposed for the RC aquifer structure based on the resulting local hydrogeological models and previous works.

Site description

Located in the northern YP, the RC is a semicircular structure approximately 180 km in diameter with a 250 km arc

(Fig. 1a). It is considered an unconfined aquifer, except for a zone with a thin, impermeable caliche layer paralleling the coast (Perry et al. 2002). Its geological composition and structure provide unique hydrogeological characteristics (Steinich and Marín 1997).

Hydrological setting

The YP aquifer has a calcareous matrix consisting of a freshwater lens that becomes progressively thinner with proximity to the coast, floating on saltwater (Marín 1990; Perry et al. 1995; Steinich and Marin 1996). Surface hydrology in the study area is defined by high bedrock permeability (Steinich and Marin 1996), and higher elevation of the inland water table relative to the sea level (Valle-Levinson et al. 2011). These factors determine aquifer flow patterns (see arrows, Fig. 1), which generally move from the Peninsula's center towards the coastal discharge areas (Pérez-Ceballos et al. 2012; Perry et al. 2002).

The RC hydrogeological structure plays a vital role in water distribution on the YP (Gómez-Nicolás et al. 2017). Its high porosity, high hydraulic conductivity and low storage capacity (Perry et al. 2002), evidenced by declining water-table elevations towards the ring (Marín 1990), makes the RC a highly permeable preferred flow pathway. The RC redistributes most of the water coming from the south to the edges (Bauer-Gottwein et al. 2011; Perry et al. 2002, 2009), allowing a small portion of water into the crater (González-Herrera and Sánchez-y-Pinto 2002). Discharge rates produced by differences between the phreatic level and sea level vary in response to marine tides and aquifer water level (Valle-Levinson et al. 2011). For millions of years, sea level changes and limestone dissolution processes have produced subsidence and cenote formation (Pope et al. 1996). Two main surface hydrogeological formations are present in the RC: cenotes and aguadas. The former contains clear water year-round and responds to aquifer water-level changes. Presence of water in the latter is uncertain, influenced by seasonal rainfall and can even disappear occasionally. Unlike cenotes, aguadas can have mud filled bottoms and aquatic vegetation at the water surface (Finch 1965) such as tule, among other plants.

High porosity allows marine water intrusion into the aquifer. The saline interface beneath the northern YP is truly extensive, reporting from 90 to 100 km inland (Steinich and Marín 1997). Interface depths find good agreement with the Ghyben-Herzberg principle (Marín 1990), computed as $s = -40 h$, where h is the water level above mean sea level (Ghyben 1888; Herzberg 1901; Hubbert 1940). Depths range from 18 to 110 m inland in the northern YP (Steinich and Marin 1996) with deviations probably caused by conduit networks showing shallower interface depth (Bauer-Gottwein et al. 2011). Perry et al. (2002) showed that the ion chemistry of the fresh groundwater lens of the northern YP is controlled by dissolution of calcium carbonate and by mixing with the

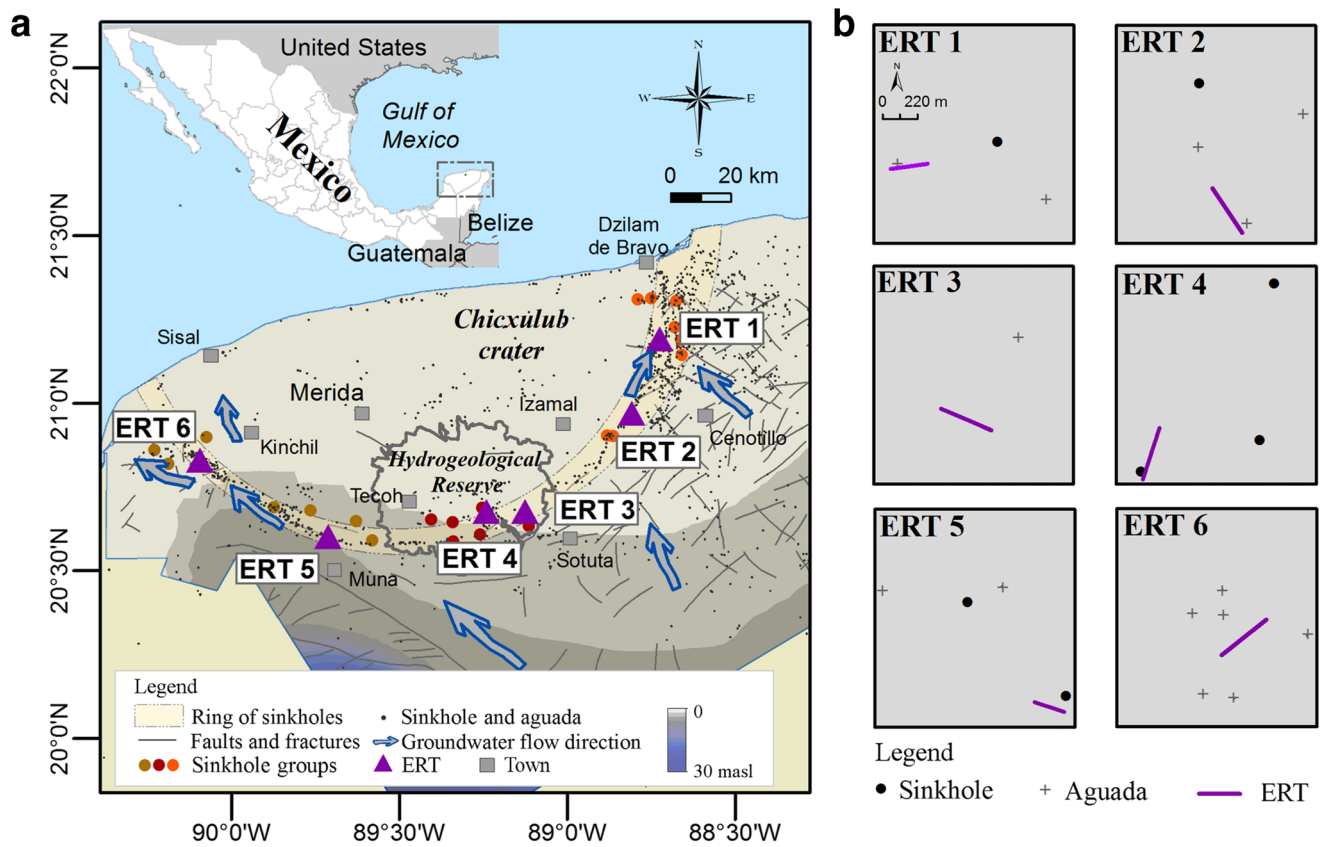


Fig. 1 **a** Hydrological map of the state of Yucatan and **b** ERT section locations. Hydrological map shows: static water level on grey-blue background (POETY 1999); cenotes and aguadas (black dots) identified visually on high-resolution satellite imagery (CNES-SPOT and Quickbird, accessed through Google Earth); cenotes shape from POETY (2007); fault and fracture systems shown with grey lines (INEGI 2002); main

water-flow direction with blue arrows (Perry et al. 2009); and cenotes grouping (brown, red and orange dots) by water physicochemical characteristics (Pérez-Ceballos et al. 2012). The ERT section locations are shown relative to nearby cenotes and aguadas from a geographic information system database (**b**)

underlying saline intrusion. The saline intrusion is younger from southeast to northwest with incorporation of modern seawater, and there is upwelling of water of an underlying saline intrusion with mixing of saline and channelized groundwater to the northeast (Perry et al. 2009). Recently conducted multivariate analyses established that there are at least three regions identified from groups of cenotes that share water chemistry and physicochemical characteristics and, therefore may be connected. These cenotes groupings (Fig. 1) are located (1) to the east, associated with seawater intrusion and sulfate originating in the southern Yucatan (brown dots), (2) in the west, with higher pH values, high hydrochemical variability and less seawater intrusion (orange dots), and (3) in the south of the RC, identified by recharge zone, with weak influence from seawater and lower electrical conductivity (red dots; Pérez-Ceballos et al. 2012).

Geological setting

On the YP, the aquifer lies beneath a low-elevation calcareous platform (Perry et al. 1995; Rebolledo-Vleyra et al. 2000)

composed mainly of limestone, dolomites and evaporites reaching thicknesses of 1,500 m (Weidie 1985). The current conceptual geological framework for the RC is based on cores drilled over the past 40 years (Fig. 2). In the 1970s, Petroleos Mexicanos (PEMEX) drilled a series of cores, followed by the National Autonomous University of Mexico (Universidad Nacional Autónoma de México - UNAM) in the 1990s, and then the International Continental Drilling Project (ICDP), and Expedition 364 of the International Ocean Discovery Program (IODP) in 2016. Of the many cores extracted on the emerged platform as part of these projects (Fig. 2), two (U2 and U8) are within the RC (Rebolledo-Vleyra et al. 2000).

In the northern YP, the aquifer extends beneath the sedimentary fill in the Chicxulub Crater, created by the impact of an approximately 10 km diameter meteorite (Pope et al. 1996). The impact basin is approximately 1 km deep and 145 km in diameter, and is filled with Cenozoic sedimentary rocks (Morgan and Warner 1999). Stratigraphic columns show sequences of almost horizontal dolomites, limestone and marls spanning from the Paleocene to the Holocene. Exposed surface rock is carbonate sedimentary, and of progressively

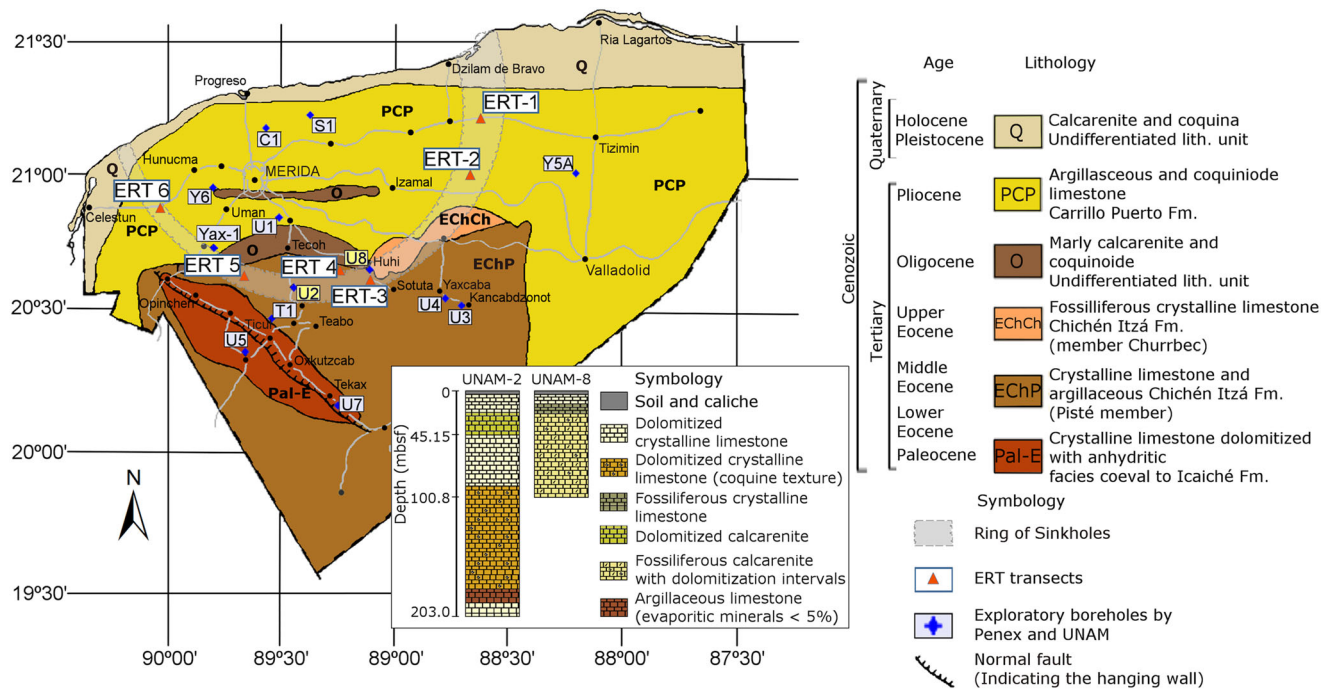


Fig. 2 Geologic map showing cores collected in the state of Yucatan as part of the UNAM scientific drilling program (wells U1–U8), one ICDP well (Yax-1) and various PEMEX wells. The RC lithology up to 200 m

below sea floor (mbsf) is shown from lithologic columns U2 and U8 borehole (modified from Rebolledo-Vieyra et al. 2000)

younger age towards the north, ranging from the Upper Cretaceous to the Holocene (Fig. 2; Rebolledo-Vieyra et al. 2000).

The impact basin’s external edge is located along the RC (Perry et al. 1995), which is the only surface expression of the crater (Pope et al. 1996), and is surrounded by a ring-shaped fault system about 200 km deep (Gulick et al. 2008). Two cores from the RC (U2 and U8) produced a ~200-m-thick initial layer composed of calcarenites and silty limestone where the aquifer may be contained (Fig. 2). At a total of 559 m depth, the U2 column consisted of 1.7 m of soil and caliche followed by 85 m of dolomitized crystalline limestone, alternating with 14 m of dolomitized calcarenite, 95 m of fossiliferous dolomitized crystalline limestone, 10 m of clay limestone and another 10.0 m of dolomitized crystalline limestone. The U8 core was 100.8 m deep and consisted of 1.0 m of soil, followed by 6.35 m of dolomitized crystalline limestone, 6.0 m of fossil crystalline limestone (up to 30%), and 87.5 m of fossiliferous calcarenite alternating with dolomitized calcarenite and a denser fossil assemblage (Rebolledo-Vieyra et al. 2000).

Site selection

Selection of sites for ERT surveys was done using the cenote database of the Yucatan state Ministry of Urban Development and the Environment (POETY 2007), completed with the cenotes and aguadas point layer identified visually on high-

resolution satellite imagery (CNES-SPOT, and Quickbird, accessed through Google Earth). In those images, the aguadas were distinguished from the cenotes by identifying bodies of water covered by hydrophilic vegetation and ground-truthed at the selected sites.

Six sites were chosen for generating ERT profiles over cenotes and aguadas, and at different distances from them (Fig. 1). The sites selected closest to the coast are ERT-1 and ERT-6, 30 km distant, with saline interface depths from 60 m, and ERT-2, 50 km from the coast, with saline interface depths from 70 m according to the Ghyben-Herzberg principle. The other sites, ERT-3, ERT-4 and ERT-5, are 70 km from the coast interface with depths at 80 m according to this principle. Interface depths may vary due to networks of fractures and vertical movements that produce a mixture of fresh and salt water (Bauer-Gottwein et al. 2011).

The resistivity profile orientation of the cenotes and aguadas are presented in Fig. 1b. ERT-4 passes over the cave of a sunken cenote, and ERT-5 was placed 50 m from an open cenote. Both transects were done along vehicle tracks through vegetation. ERT-4, running southwest–northeast, was located some 800 m from cenotes on either side of the transect. At ERT-5, oriented west–east, one cenote was 50 m from the transect, and an aguada was 700 m away.

Aguadas were explored at site ERT-1, along the edge of an aguada, and at ERT-2, which was located 20 m from the edge of an aguada. Transect ERT-1 was oriented west–east, and cenotes and other aguadas were 800 m away. ERT-2 was

oriented northwest–southeast at 20 m from the edge of an aguada, with cenotes and other aguadas about 600 m distant.

Transects ERT-3 and ERT-6, both oriented west–east, were intended to explore the aquifer far from cenotes and aguadas. At ERT-3, the only such structure within a 2 km radius was an aguada. Transect ERT-6 was located within a semicircle of aguadas at an average distance of 500 m.

Techniques

ERT measurements

Geophysical techniques have been successfully applied in exploration of subterranean waters, and ERT is one of the most widely used (Loke et al. 2013). It has been applied in characterization of aquifer geological structures (Bechtel et al. 2007; Griffiths and Barker 1993), structure of surface karst formations (e.g. Stepišnik and Mihevc 2008), location of flooded conduits (e.g. Gómez-Nicolás et al. 2017; Zhu et al. 2011) and the study of saltwater intrusion (e.g. de Franco et al. 2009; Nguyen et al. 2009).

Optimum electrode configuration and spacing for mapping different characteristics in ERT studies has been widely discussed by Dahlin and Zhou (2004), Loke (2001), Samouëlian et al. (2005), Yang and Wang (2015), and Zhu et al. (2011). In the present study, the dipole–dipole array was used because it provides good information for mapping of vertical structures such as dykes and cavities (Loke 2001; Samouëlian et al. 2005; Zhou et al. 2002; Yang and Wang 2015). Good results have been reported for ERT in karstic systems, and such results demonstrate the capacity of the dipole–dipole array to map structure (Gómez-Nicolás et al. 2017; Stepišnik and Mihevc 2008). Indeed, this array is used for delineating potential cenotes and collapsed areas (Zhou et al. 2002).

Resistivity acquisition

Six ERT profiles were obtained between July and September 2015 in a cenote, an aguada and four nearby areas within the RC. All were done using two-dimensional (2D) ERT. Electrical resistivity was measured with a SuperSting R1/IP Controller, connected to a switch box (Advanced Geosciences Inc. 2005) using a 345 m-long stationary cable with 70 electrodes, with 5 m between electrodes. At sites ERT-1 and ERT-5, only half the cable length was used due to difficult access to surrounding terrain. Data quality was ensured by measuring electrode contact before taking measurements, and resetting any electrodes exhibiting a contact resistance $>2,000 \Omega$ (Deraedt et al. 2015; Loke et al. 2013; van Beynen 2011). Electrodes were moistened with saltwater to improve contact with the soil and improve current injection. Each resistivity

measurement was based on two measurement cycles, with a 2% maximum error and a maximum repeat error of 2%. A total of 619 measurements were taken for profiles using 36 electrodes and 2,125 measurements for profiles with 70 electrodes. Maximum effective depth was 37 m for 36-electrode profiles and 66 m for 70-electrode profiles. Transect geometry is shown in Fig. 1 and described in the site selection section.

Data processing

The inversion of field data was performed in EarthImager 2D by Advanced Geosciences Inc. Before processing, records were filtered to remove noisy readings caused by low voltage or poor electrode contact-resistance ratio (Loke et al. 2013; Wilkinson et al. 2008). Any values that were negative, $<1 \Omega\text{m}$ or $>10,000 \Omega\text{m}$ were eliminated. In some transects, the data from effective depths greater than 30 m were noisy; therefore, 30 m was set as the lower depth for inversion of all the ERT profiles to ensure good quality data. The resistivity model inversion was calculated using the bidimensional partial differential equation in the Fourier transformed domain. The equation was resolved with EarthImager2D using the finite elements and robust inversion method (Claerbout and Muir 1973). From this model, predicted apparent resistivities were calculated and compared to the actual field apparent resistivities. The root mean square (RMS) was used to compare the field data to the predicted data based on the model.

Structure determination

Porosity and content of water within the lithology, in this particular context, produces very large resistivity contrast, $>1,000 \Omega\text{m}$ for dry limestone, to $<100 \Omega\text{m}$ in limestone saturated with freshwater. Other available resources are essential to constrain ERT interpretation. For example, different structural components in karst systems have different signatures (Table 1); dry or unsaturated limestone produces resistivity values from $1,000 \Omega\text{m}$ up to $100,000 \Omega\text{m}$ (Palacky 1988; Stepišnik 2008; Zhou et al. 2002), while unsaturated limestone with presence of other materials such as alluvial deposits, produces lower resistivity of $500\text{--}2,500 \Omega\text{m}$ (Keshavarzi et al. 2016). When the unsaturated weathered/fractured bedrock are wet, lower resistivity ranges are reported, varying from 200 to $1,000 \Omega\text{m}$ (Stepišnik 2008), to $100\text{--}500 \Omega\text{m}$ (Keshavarzi et al. 2016).

As mentioned before, fractures, dissolution cavities and primary porosity are the main characteristics of the rock matrix. In turn, fluids content (air, freshwater or saltwater) will account for the resistivity response of the formation; the ionic difference in content between freshwater and saltwater will generate a resistivity contrast of at least one order of magnitude.

Table 1 Comparative resistivity values for caves or conduits, and saturated and unsaturated fractures in karstic systems

Structural components	Inverted resistivity (Ωm)	Reference
Unsaturated limestone	1,000–100,000	Palacky (1988)
	1,000	Zhou et al. (2002)
	500–2,500	Keshavarzi et al. (2016)
Fractured unsaturated limestone	100–500	Keshavarzi et al. (2016)
	200–1,000	Stepišnik (2008)
Fractured freshwater-saturated limestone	10–100	Loke et al. (2001)
	<250	Telford and Sheriff (1990)
Freshwater-saturated caves or conduits	5–15	Keshavarzi et al. (2016)
	6–12	Pérez-Ceballos et al. (2012)
	1–47	Gómez-Nicolás et al. (2017)

Increased resistivity in fracture fill can be caused by air, and decreased resistivity by conductive materials. Fracture fill can include depositional materials such as grains or clay of different textures and sources (Dunham 1962), which generate variations in conductivity in response to grain size and composition. Dry cavities and limestone blocks can be detected by their high resistivity (Telford and Sheriff 1990).

Matrix resistivity decreases when saturated with water. Water-saturated limestone generates typical values 10–100 Ωm (Loke 2001), and can be as low as $\sim 5 \Omega\text{m}$ when in conduits (Keshavarzi et al. 2016; Zhu et al. 2011). In the study area, large pores (>1 m) flooded with freshwater generates values 6–12 Ωm (Pérez-Ceballos et al. 2012), but can range from 1 to 47 Ωm in saturated conduits (>5 m) (Gómez-Nicolás et al. 2017). These values can vary depending on conduit size, degree of rock fracturing and presence of calcareous material deposition—for example, saturated limestone containing clay can generate values similar to the $\sim 250 \Omega\text{m}$ reported for silty materials (Telford and Sheriff 1990). Given the high contrast of resistivity shown in different studies, the initial conceptual model for this study area consists of three layers (Table 2).

Results

Electrical resistivity tomography: local geoelectrical models

Data from the six geoelectrical explorations in the RC allowed creation of profiles for each transect which represent three general areas: areas near cenotes, ERT-4 and ERT-5 (Fig. 3a); areas near aguadas, ERT-1 and ERT-2 (Fig. 3b); and areas far from these structures, ERT-3 and ERT-6 (Fig. 3c). Resistivity profiles recorded are showed in Fig. 3 (left panel) and local geoelectrical models from the results, presented in Table 3, are shown in Fig. 3 (right panel). The RMS for the resulting models was $\sim 10\%$ for ERT-1, ERT-2, ERT-4 and ERT-5, supporting these results as feasible solutions, whereas

for ERT-3 and ERT-6, considering the poor contact-resistance ratio and the higher heterogeneity, the $\sim 20\%$ RMS as was considered reasonable, always acknowledging that deeper information from the ERT becomes less reliable.

From the ERT, the geoelectrical structure of the area was classified into four well-defined geoelectrical units (Table 3). The profiles from areas with cenotes (Fig. 3a) show areas where LRI has a larger area than areas far from these formations (Fig. 3c). Located in the southern RC, the ERT-4 resistivity profile depicts LR II (<100 Ωm) separated by LRI (<200 Ωm) under HRI (<25,000 Ωm). Transect ERT-5 was 50 m from a cenote and oriented to an aguada, and shows a LR II of 8 m (<40 Ωm) under a HR II (<7,000 Ωm). Both these profiles present high porosity, suggesting the possibility of connections between cenotes and other surface structures such as aguadas by the network of fractures.

Of the two profiles from aguadas (Fig. 3b), ERT-1, in the east RC, depicts an aguada in the first portion of the transect and its connection to the aquifer. The aguada's body of water (LR II) occurs within the first 20–40 m of the transect, extends at least 20 m deep, and is bordered by LRI. Conduits LR II (<100 Ωm) are separated by LRI (<200 Ωm) under a HR II (200–5,000 Ωm). The ERT-1 profile suggests that aguadas may be connected to a fracture network within the aquifer. This profile is similar to that of ERT-4 and ERT-5, meaning they may have similar origins. The ERT-2 profile was conducted along a road built with rock and sand, which parallels an aguada. All along this transect is LRI ($\sim > 100 \Omega\text{m}$) under the transition to HR II (500–9,000 Ωm).

Table 2 Conceptual resistivity model

Rock	Thickness (m)	Resistivity (Ωm)
Dry limestone	5	1,000
Limestone saturated with freshwater	20	100
Limestone saturated with saltwater	Semi-space	10

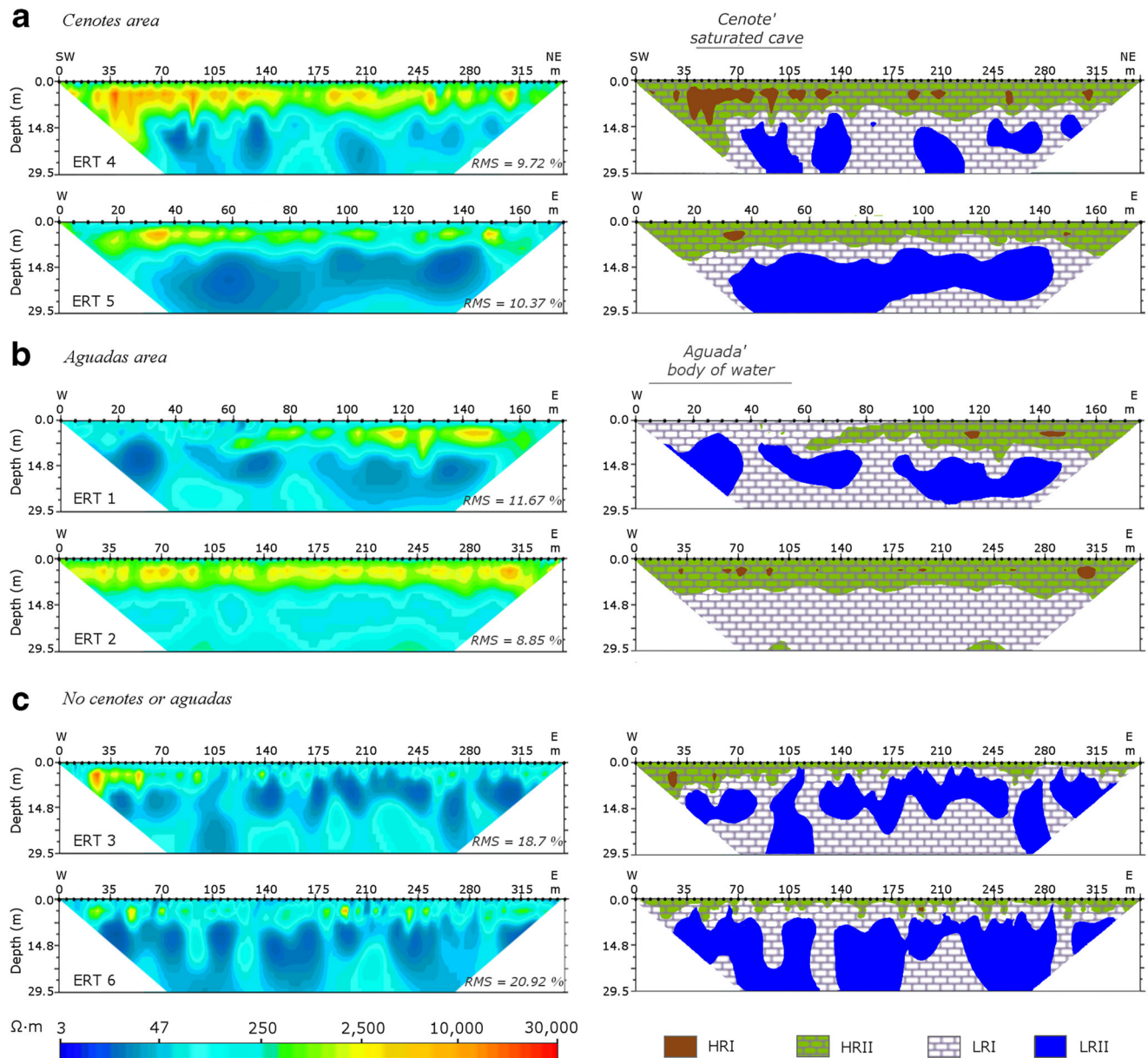


Fig. 3 Resistivity profiles recorded along six ERT transects with inverted resistivity (left panel) and local geoelectrical models from the geoelectrical units (Table 3) (right panel). **a** Presents a cenotes area with

a profile over a cenote cave and 50 m away; **b** Aguadas area, with profile of an aguada and 20 m away, and **c** no cenotes or aguadas within 500 m

From transects removed from cenotes and aguadas (Fig. 3c), the ERT-6 profile shows LR II (3–40 Ωm) within LRI (~160 Ωm) under a transition from LRI to HR II (100–

7,000 Ωm). The relatively low resistivity in the ERT-6 HR II (>200 Ωm) may be due to groundwater level being closer to the surface in areas nearer the coast, and the platform’s low elevation. A very similar profile was recorded in ERT-3, an area without cenotes and only one aguada within a 2-km radius. Similar to previous results, there are LR II (3–40 Ωm) within a saturated LRI (50–200 Ωm) under the transition from LRI to HRI (200–23,000 Ωm). As in ERT-6, LRI in ERT-3 appears to be of smaller area than those nearer cenotes and aguadas, suggesting an aquifer interconnected by a system of fractures with less resistivity in proximity to these formations.

Table 3 Geoelectrical structure of the study area

Name	Resistivity
High resistivity unit I (HRI)	>3,000 Ωm
High resistivity unit II (HR II)	300–2,900 Ωm
Low resistivity unit I (LRI)	100–250 Ωm
Low resistivity unit II (LR II)	<100 Ωm

The contrast between the profiles over and near cenotes and aguadas, and those far from these formations, suggests that the presence of these formations may be indicative of greater hydraulic conductivity in areas around them. Cenotes and aguadas may therefore be a surface expression of a network of conduits and caves throughout the RC formed by erosion, dissolution and fracturing of the surface limestone layers.

Ring of Cenotes regional conceptual model

Several authors have proposed different conceptual models to explain the origin of the RC. The most accepted hypothesis is the differential elevation between the background terrain and the sedimentary basin by means of the subsidence, what Melosh (1989) called “gravitational accommodation” (Rebolledo-Vieyra et al. 2010; Pope et al. 1996), generating a system of faults that accommodate the differential sinking through the weak zones at the edge of the crater. Nonetheless, other authors have proposed the origin of the RC as the result of post-impact development of a reef barrier at the edge of the crater (Perry et al. 2002); however, no strong evidence for the latter has ever been reported.

The interpretation presented here is based on the conceptual model proposed by Rebolledo-Vieyra et al. (2010) and local geoelectrical models to conceptualize a regional model for the RC (Fig. 4). It proposes that the aquifer exists in a fractured limestone matrix with two main zones: the vadose zone, consisting of geoelectrical units HRII to HRI (~300–25,000 Ω m), and the overlying LRII zone, which is interpreted here as the aquifer (<100 Ω m), separated by LRI transition unit HR II.

Valle-Levinson et al. (2011) have advanced a conceptual model of the coastal area, consisting of a fracture zone associated with a network of caves or conduits interconnected via fracture systems connected to the sea. This internal structure is expressed on the surface as cenotes and aguadas created by

erosion of the surface limestone layers. Fractures in the network’s matrix can range from microfractures (<1 m) to conduits measuring various meters in width. Aguadas differ from cenotes in that hydrophilic vegetation has invaded the water surface. Finally, the entire aquifer is connected through this matrix to the sea.

The freshwater lens that constitutes the aquifer flows over marine-water intrusion penetrating the limestone matrix (Marín 1990). Because the marine-water intrusion has been reported up to 90 km inland from the coast (Steinich and Marin 1997), the model assumes that it underlays the entire study area. The main hydraulic conductivity characterizing the RC (Null et al. 2014) is represented by flow lines in a system of west–east fractures, according to the orientation of the models produced from the ERT profiles. Increased static water levels with distance from the coast (POETY 1999), and submarine discharge of the aquifer caused by pressure from the water column on marine-water intrusion, are shown at both extremes of the RC (Valle-Levinson et al. 2011).

Discussion

The geological origin of a karstic aquifer generates a very complex and heterogeneous porous and permeable system. Many studies have tried to represent this structure (Borghi et al. 2012), but this has been particularly challenging on the YP due to lack of detailed geological data and limitations of conventional techniques in exploring karst structures (Vuilleumier et al. 2013).

Cenotes and aguadas are the surface formations that characterize and define the RC as a hydrogeological structure. Better understanding of these surface features has been hampered by the difficulty of exploratory SCUBA diving in cenotes, the matrix’s heterogeneous fracture system and the

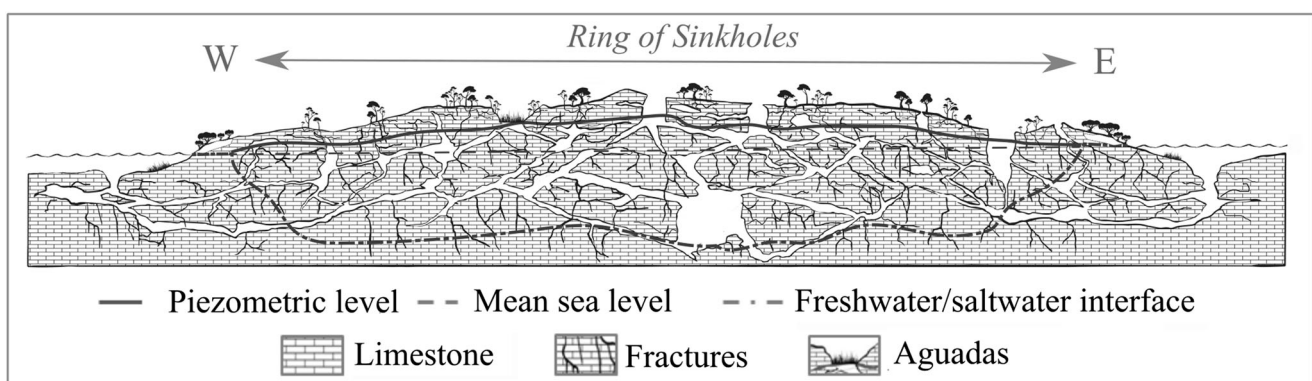


Fig. 4 Regional conceptual model of the coastal aquifer at the RC from west to east. The aquifer is interconnected between caves and conduits through limestone with varying degrees of fracturing under an almost flat fractured vadose zone. Freshwater level is shown as a continuous line (POETY 1999), and mean sea level as a dashed line inland. The

freshwater lens of the aquifer flows over intruding marine water, and these are separated by an interface of brackish water (dot–dash line; Valle-Levinson et al. 2011; Marín 1990). The vegetation at the ends of the ring corresponds to mangroves

dense vegetation covering aguadas, which prevents access to areas near conduits and caves. In the present study, the goal was not to create a quantitative estimation of the fracture size or deposit materials. Instead, the goal was to generate a spatial structural profile based on resistivity values recorded at these two types of formations and in areas without them. This is an important initial step in understanding the RC's shallow structural pattern. The present results are a complement to studies of connectivity of local and regional flows based on geochemistry (Gómez-Nicolás et al. 2017; Pérez-Ceballos et al. 2012; Perry et al. 2002, 2009) and modelling studies (Borghini et al. 2012; Vuilleumier et al. 2013). They indicate the connectivity of aguadas to the aquifer, the similarity of resistivity values between aguadas and cenotes, and the networks of conduits and fractures that shape the aquifer over distances.

Geophysical methods have produced notable advances in the knowledge of the Chicxulub Crater (Rebolledo-Vieyra et al. 2010; Rebolledo-Vieyra and Urrutia-Fucugauchi 2006, 2004), and the directions of aquifer surface flows (Steinich and Marin 1996). Variations in resistivity show clear differences between freshwater saturated and unsaturated zones, resulting in a two-layer model for the upper aquifer: a vadose or unsaturated zone (300–25,000 Ωm) over a phreatic zone (3–250 Ωm). Electrode configuration allowed identification of conduits with resistivity values near those reported by Zhou et al. (2002), and coinciding with the resistivity ranges selected by Gómez-Nicolás et al. (2017) for the study area. The method used for the determination of the resistivity ranges of structures is a feasible method with higher correlation to the tomography results than the ranges obtained by other methods such as the conductivity measurement of a sample (Keshavarzi et al. 2016; Pérez-Ceballos et al. 2012).

The main source of information about the petrology of this region comes from studying the surficial lithology of cores recovered by scientific drilling projects down to 1,500 mbsl. Figure 2 shows the spatial distribution of the scientific boreholes (UNAM1–8 and ICDP, Yax-1) and exploratory boreholes (PEMEX S1, T1, Y5A and C1). From these missions one can derive a comprehensive understanding of the surface geology, at least on the first 400 m, well below the limit of exploration of this study.

Rebolledo-Vieyra et al. (2000) present a very detailed description of the continuous core recovered by the UNAM drilling program. Basically it consists of a sequence of different calcareous rocks, dominated by calcarenite (high porosity), crystalline limestone, thinner horizons of dolomite and some coquina (high porosity, very fragile). In all the cases, heavy fracturing, at the cm scale, was often observed. Ward et al. (1995) described the lithology from the exploratory boreholes from PEMEX, in a general sense; the geology described is very similar to that described by Rebolledo-Vieyra et al. (2000). The same situation is present with Yax-1 (Rebolledo-Vieyra and Urrutia-Fucugauchi 2004), described with a similar lithology. Dressler et al. (2003) reported the presence of large dissolution cavities within the first 40 m of the borehole.

Based on this information, the lithology was assigned to the geoelectrical units that probably will account for the geoelectrical properties. Considering the shallow stand of the phreatic level and the fact that the zone represents the present influence of saltwater intrusion, the method involved added the geoelectrical properties to the lithology that will change the resistivity response of, otherwise, dry lithologies.

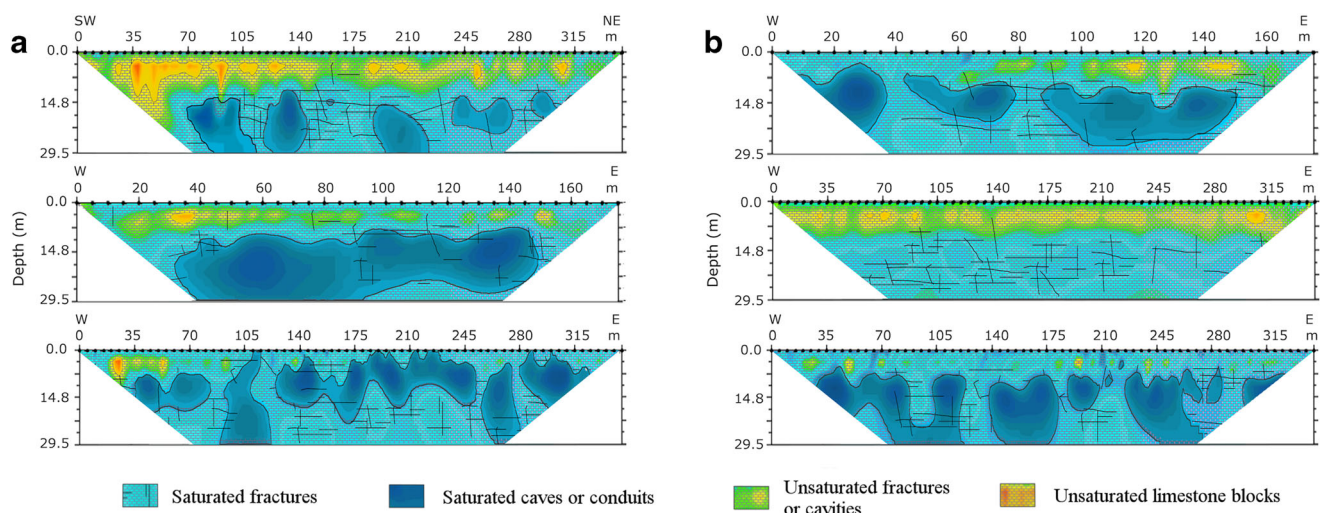


Fig. 5 Geological interpretation of geoelectrical units based on the observations of core samples and direct observations on the field. Fractured limestone is emphasized with straight black lines over a

limestone matrix, and water bodies and limestone blocks are delineated and presented without a matrix. The images are presented from shorter to longer distance to **a** cenotes and **b** aguadas

Conclusion

Electrical resistivity tomography (ERT) is effective for exploring freshwater-saturated caves, conduits and fractures in limestone matrix. Use of ERT in the study area has identified four geoelectrical units that show the limestone structure: LRI, in saturated caves and conduits, with resistivity $<100 \Omega\text{m}$; LR II, in saturated fractured limestone from 100 to $250 \Omega\text{m}$; HR II, in unsaturated cavities and fractured limestone from 250 to $3,000 \Omega\text{m}$; and HRI in limestone blocks, with resistivity $>3,000 \Omega\text{m}$. The ERT profiles accurately recorded aquifer structure at up to 30 m depth in a fractured matrix with a 3–250 Ωm resistivity range below an unsaturated zone with a 300–25,000 Ωm range. Resistivity in the bodies of water in aguadas and cenotes was $<100 \Omega\text{m}$ ($\sim 47 \Omega\text{m}$), and these were separated from other conduits or bodies of water by limestone with different degrees of fracturing and with resistivity values $<250 \Omega\text{m}$. The interpretation is presented in Fig. 5.

The similarity in resistivity values between aguadas and cenotes may indicate that they have similar structures and/or origins. In turn, these data can function as a complement to future exploration aimed at expanding the range of recorded resistivity and better understanding the structural complexity of cenotes and aguadas for development of mathematical models.

The main limitation of the ERT, especially in terrains like Yucatán, where lack of access to outcrops or other means of direct observations of the geology are difficult, prevents a statistically significant ground-truthing. The conduits recorded near cenotes and aguadas are of larger diameter than in areas further away, suggesting that these formations are surface expressions of the aquifer's internal structure of caves and conduits (Fig. 5). In the RC, presence of cenotes and aguadas may indicate greater hydraulic conductivity in the area around them.

Fracturing in the system may be related to preferential flow patterns and higher hydraulic conductivity within the RC. Water flow towards the edges of the RC and its discharge into the sea suggest that conduits and fracture systems in the RC are oriented largely in the west–east direction.

Acknowledgements Thanks are due A. I. Muñiz-Castillo, M. Lopez, J. G. Rojas, G. Santos and A. Valdez-Cibrian for their help with the field work, and J. A. Trinidad for assistance with graphic design. We would like to thank J. Lindsay-Edwards for English editing and Lewis Land, Timothy D. Bechtel and Jean-Michel Lemieux for comments that helped to significantly improve the manuscript.

Funding information The research reported here was financed by the Consejo Nacional de Ciencia y Tecnología through a grant to M.R-V (CONACyT No. 247565) and a PhD scholarship (No. 340292) to L. A-G.

References

- Advanced Geosciences Inc (2005) Instruction Manual for Earth-Imager 2D. Resistivity and IP Inversion Software. Copyright (2002–2009). Advanced Geosciences, Austin, TX
- Anderson MP, Woessner WW (1992) Applied groundwater modeling: simulation of flow and advective transport. Academic, San Diego
- Bauer-Gottwein P, Gondwe BR, Charvet G, Marín LE, Rebolledo-Vieyra M, Merediz-Alonso G (2011) Review: the Yucatán Peninsula karst aquifer. *Mexico Hydrogeol J* 19(3):507–524. <https://doi.org/10.1007/s10040-010-0699-5>
- Bechtel TD, Bosch FP, Gurk M (2007) Geophysical methods. In: Goldscheider N, Drew D (eds) *Methods in karst hydrogeology*, CRC P, Boca Raton, FL, pp 171–199
- Borghi A, Renard P, Jenni S (2012) A pseudo-genetic stochastic model to generate karstic networks. *Hydrol J* 414:516–529. <https://doi.org/10.1016/j.jhydrol.2011.11.032>
- Claerbout JF, Muir F (1973) Robust modeling with erratic data. *Geophysics* 38(5):826–844. <https://doi.org/10.1190/1.1440378>
- Dahlin T, Zhou B (2004) A numerical comparison of 2D resistivity imaging with ten electrode arrays. *Geophys Prospect* 52:379–398. <https://doi.org/10.1111/j.1365-2478.2004.00423.x>
- de Franco R, Biella G, Tosi L, Teatini P, Lozej A, Chiozzotto B, Giada M, Rizzetto M, Claude C, Mayer A, Bassan V, Gasparetto-Stori G, Bassan V (2009) Monitoring the saltwater intrusion by time lapse electrical resistivity tomography: the Chioggia test site (Venice Lagoon, Italy). *J Appl Geophys* 69(3):117–130. <https://doi.org/10.1016/j.jappgeo.2009.08.004>
- Decree 117 (2018) Decreto 117, decreto que establece el área natural protegida denominada reserva estatal geohidrológica del anillo de cenotes. Gobierno del estado de Yucatán [Decree 117, decree establishing the protected natural area called the hydrogeological state reserve of the Ring of Cenotes. Government of the state of Yucatán]. http://www.yucatan.gob.mx/gobierno/diario_oficial.php?f=2013-10-28. Accessed January 2018
- Delgado-Rodríguez O, Campos-Enriquez O, Urrutia Fucugauchi J, Arzate JA (2001) Occam and Bostick 1-D inversion of magnetotelluric soundings in the Chicxulub impact crater, Yucatán, Mexico. *Geofis Int* 40(44):271–283. <https://doi.org/10.19155/geofint.2001.040.4.410>
- Deraedt D, Touzé D, Robert T, Colinet G, Degré A, Garré S (2015) Contact resistance problems applying ERT on low bulk density forested stony soils. Is there a solution? In: EGU General Assembly conference abstracts, ID 5795, Vienna, 17 April, 2015
- Dressler BO, Sharpton VL, Morgan J, Buffler R, Moran D, Smit J, Stoffer D, Urrutia J (2003) Investigating a 65-ma-old smoking gun: deep drilling of the Chicxulub impact structure. *EOS Trans Am Geophys Union* 84(14):125–121. <https://doi.org/10.1029/2003EO140001>
- Dunham RJ (1962) Classification of carbonate rocks according to depositional textures. *Memoir American Petroleum Geologist*, GeoScienceWorld, McLean, VA
- Fairchild IJ, Baker A (2012) Scientific and geological context. In: Fairchild IJ, Baker A (eds) *Speleothem science: from process to past environments*. Blackwell, Oxford, pp 3–27
- Finch WA (1965) The karst landscape of Yucatan. PHD Thesis, University of Illinois, Urbana, IL, USA
- Fitchen WM, Starcher MA, Buffler RT, Wilde GL (1995) Sequence Stratigraphic framework of Lowe Permian carbonate platform margins, Sierra Diablo, West Texas. In: Garber R (ed) *Wolfcampian-Leonardian shelf margin facies of the Sierra Diablo: seismic models for subsurface exploration*. West Texas Geological Society, Midland, TX, pp 23–66
- Ford D, Williams PD (2013) *Karst hydrogeology and geomorphology*. Wiley, Chichester, UK

- Gómez-Nicolás M, Rebolledo-Vieyra M, Canto-Lugo E, Huerta-Quintanilla R, Ochoa-Sandoval P (2017) Connectivity in a karst system using electrical resistivity tomography and network theory. *Groundwater* 56(5):732–741. <https://doi.org/10.1111/gwat.12618>
- González-Herrera RI, Sánchez-y-Pinto G-VJ (2002) Groundwater-flow modeling in the Yucatan karstic aquifer, Mexico. *Hydrogeol J* 10: 539–552. <https://doi.org/10.1007/s10040-002-0216-6>
- Ghyben WB (1888) Nota in Verband met de Voorgenomen put boring Nabij Amsterdam [Note in connection with the proposed well drilling near Amsterdam]. *Tijdschrift Kononklijk Institut Ing* 9:8–22
- Griffiths DH, Barker RD (1993) Two-dimensional resistivity imaging and modelling in areas of complex geology. *J Appl Geophys* 29(3):211–226. [https://doi.org/10.1016/0926-9851\(93\)90005-J](https://doi.org/10.1016/0926-9851(93)90005-J)
- Gulick SPS, Barton PJ, Christeson GL, Morgan JV, McDonald M, Mendoza-Cervantes K, Pearson ZF, Surendra A, Urrutia-Fucugauchi J, Vermeesch PM, Warner MR (2008) Importance of pre-impact crustal structure for the asymmetry of the Chicxulub impact crater. *Nature Geosci* 1(2):131–135. <https://doi.org/10.1038/ngeo103>
- Herzberg A (1901) Die Wasserversorgung einiger Nordseebäder [The water supply of some spas on the North Sea]. *J Gasbeleuch Wasserversorg* 44:815–819
- Hubbert MK (1940) The theory of ground-water motion. *J Geol* 48(8): 785–944. <https://doi.org/10.1086/624930>
- INEGI (2002) Instituto Nacional de Estadística y Geografía, Conjunto de datos vectoriales Geológicos, fallas y fracturas [National Institute of Statistics and Geography, Geological vector data set, faults and fractures]. Escala 1:1 000 000 (Continuo Nacional). INEG, Aguascalientes, Mexico
- Keshavarzi M, Baker A, Kelly BF, Andersen MS (2016) River-groundwater connectivity in a karst system, Wellington, New South Wales, Australia. *Hydrogeol J* 25(2):557–574. <https://doi.org/10.1007/s10040-016-1491-y>
- Loke MH (2001) Electrical imaging surveys for environmental and engineering studies: a practical guide to 2-D and 3D surveys. RES2DINV Manual. IRIS Instruments. www.iris-instruments.com. Accessed June 2019
- Loke MH, Chambers JE, Rucker DF, Kuras O, Wilkinson PB (2013) Recent developments in the direct-current geoelectrical imaging method. *J Appl Geophys* 95:135–156. <https://doi.org/10.1016/j.jappgeo.2013.02.017>
- Marín LE (1990) Field investigations and numerical simulation of groundwater flow in the karstic aquifer of northwestern Yucatan, Mexico. PhD Thesis, Northern Illinois University, USA
- Melosh HJ (1989) Impact cratering: a geologic process. Research supported by NASA, vol 11. Oxford University Press, New York, 253 pp
- Morgan J, Warner M (1999) Chicxulub: the third dimension of a multiring impact basin. *Geology* 27(5):407–410. [https://doi.org/10.1130/0091-7613\(1999\)027<0407:CTTDOA>2.3.CO;2](https://doi.org/10.1130/0091-7613(1999)027<0407:CTTDOA>2.3.CO;2)
- Nguyen F, Kemna A, Antonsson A, Engesgaard P, Kuras O, Ogilvy R, Gisbert J, Jorretto S, Pulido-Bosch A (2009) Characterization of seawater intrusion using 2D electrical imaging near surface. *Geophysics* 7(1303):377–390. <https://doi.org/10.3997/1873-0604.2009025>
- Null KA, Knee KL, Crook ED, de Siewes R-VM, Hernández-Terrones L, Paytan A (2014) Composition and fluxes of submarine groundwater along the Caribbean coast of the Yucatan Peninsula. *Cont Shelf Res* 77:38–50. <https://doi.org/10.1016/j.csr.2014.01.011>
- Palacky GJ (1988) Resistivity characteristics of geologic targets. In: Nabighian MN (ed) *Electromagnetic methods in applied geophysics*. Society of Exploration Geophysicists, Tulsa, OK, pp 53–129. <https://doi.org/10.1190/1.9781560802631.ch3>
- Pérez-Ceballos P-ÁRJ, Euán-Ávila JI, Hernández-Arana H (2012) Regionalization based on water chemistry and physicochemical traits in the Ring of Cenotes, Yucatán, México. *J Cave Karst Stud* 74(1):90–102. <https://doi.org/10.4311/2011es0222>
- Perry E, Marín LE, McClain J, Velazquez G (1995) Ring of Cenotes (sinkholes) Northwest Yucatan, Mexico: its hydrogeologic characteristics and possible association with the Chicxulub impact crater. *Geology* 23(1):17–20. [https://doi.org/10.1130/0091-7613\(1995\)023<0017:ROCSNY>2.3.CO;2](https://doi.org/10.1130/0091-7613(1995)023<0017:ROCSNY>2.3.CO;2)
- Perry E, Velazquez-Oliman G, Marín L (2002) The hydrogeochemistry of the karst aquifer system of the northern Yucatan Peninsula, Mexico. *Int Geol Rev* 44(3):191–221. <https://doi.org/10.2747/0020-6814.44.3.191>
- Perry E, Paytan A, Pedersen B, Velazquez-Oliman G (2009) Groundwater geochemistry of the Yucatan peninsula, Mexico: constraints on stratigraphy and hydrogeology. *J Hydrol* 367(1–2):27–40. <https://doi.org/10.1016/j.jhydrol.2008.12.026>
- POETY (1999) Programa de Ordenamiento Ecológico Territorial del Estado de Yucatán. Conjunto de datos vectoriales con el nivel estático del agua [Program of Territorial Ecological Management of the State of Yucatan Vector data set with static water level]. <http://bitacoraordenamiento.yucatan.gob.mx>. Accessed January 2015
- POETY (2007) Programa de Ordenamiento Ecológico Territorial del Estado de Yucatán. Conjunto de datos vectoriales de cenotes [Program of Territorial Ecological Management of the State of Yucatan Sinkhole vector data set]. <http://bitacoraordenamiento.yucatan.gob.mx>. Accessed January 2015
- Pope KO, Ocampo AC, Kinsland GL, Smith R (1996) Surface expression of the Chicxulub crater. *Geology* 24(6):527–530. [https://doi.org/10.1130/0091-7613\(1996\)024<0527:SEOTCC>2.3.CO;2](https://doi.org/10.1130/0091-7613(1996)024<0527:SEOTCC>2.3.CO;2)
- Rebolledo-Vieyra M, Urrutia-Fucugauchi J (2004) Magnetostratigraphy of the impact breccias and post-impact carbonates from borehole Yaxcopoil-1, Chicxulub impact crater, Yucatán, Mexico. *Meteorit Planet Sci* 39(6):821–829. <https://doi.org/10.1111/j.1945-5100.2004.tb00932.x>
- Rebolledo-Vieyra M, Urrutia-Fucugauchi J (2006) Magnetostratigraphy of the cretaceous/tertiary boundary and early Paleocene sedimentary sequence from the Chicxulub impact crater. *Earth Planets Space* 58(10):1309–1314. <https://doi.org/10.1111/j.1945-5100.2004.tb00932.x>
- Rebolledo-Vieyra M, Urrutia-Fucugauchi J, Marín LE, Trejo-García A, Sharpton VL, Soler-Arechalde AM (2000) UNAM Scientific Shallow-Drilling Program of the Chicxulub impact crater. *Int Geol Rev* 42(10):928–940. <https://doi.org/10.1080/00206810009465118>
- Rebolledo-Vieyra M, Urrutia-Fucugauchi J, López-Loera H (2010) Aeromagnetic anomalies and structural model of the Chicxulub multiring impact crater, Yucatan, Mexico. *Rev Mexicana Cien Geológ* 27(1):85–195
- Rebolledo-Vieyra M, Marín LE, Sharpton VL, Trejo-García A (2011) The Chicxulub impact crater and its influence on the regional hydrology in northwestern Yucatan, Mexico. In: Buster NA, Norris R (eds) *Gulf of Mexico origin, waters, and biota*, vol 3. Texas A&M University Press, College Station, TX, pp 279–290
- Samouëlian A, Cousin A, Tabbagh A, Bruand A, Richard G (2005) Electrical resistivity survey in soil science: a review. *Soil Tillage Res* 83:173–193. <https://doi.org/10.1016/j.still.2004.10.004>
- Schmitter-Soto JJ, Escobar-Briones E, Alcocer J, Suárez-Morales E, Elías-Gutiérrez M, Marín, LE (2002) Los cNotes de la Península de Yucatán [The Cenotes of the Yucatan Peninsula]. In: de La Lanza G, García Calderón JL (Ed) *Lagos y presas de México [Lakes and dams of Mexico]*, AGT, Mexico City, pp 337–381
- Steinich B, Marín LE (1996) Hydrogeological investigations in northwestern Yucatan, Mexico, using resistivity surveys. *Groundwater* 34(4):640–646. <https://doi.org/10.1111/j.1745-6584.1996.tb02051.x>
- Steinich B, Marín LE (1997) Determination of flow characteristics in the aquifer of the northwestern Peninsula of Yucatan, Mexico.

- Hydrology J 191(1):315–331. [https://doi.org/10.1016/S0022-1694\(96\)03038-7](https://doi.org/10.1016/S0022-1694(96)03038-7)
- Stepišnik U (2008) The application of electrical resistivity imaging in collapse doline floors: Divača karst, Slovenia. *Stud Geomorphol Carpatho-Balcanica* 42:41–56
- Stepišnik U, Mihevc A (2008) Investigation of structure of various surface karst formations in limestone and dolomite bedrock with application of the electrical resistivity imaging. *Acta Carsolog* 37(1):133–140. <https://doi.org/10.3986/ac.v37i1.165>
- Telford WM, Sheriff RE (1990) *Applied geophysics*, vol 1. Cambridge University Press, Cambridge
- Toran L, Herman E, White B (2007) Comparison of flowpaths to a well and spring in a karst aquifer. *Groundwater* 45(3):281–287
- Valle-Levinson A, Marino-Tapia I, Enriquez C, Waterhouse AF (2011) Tidal variability of salinity and velocity fields related to intense point-source submarine groundwater discharges into the coastal ocean. *Limnol Oceanogr* 56(4):1213–1224. <https://doi.org/10.4319/lo.2011.56.4.1213>
- van Beynen PE (2011) *Karst management*. Springer, Heidelberg, Germany
- Vuilleumier C, Borggi A, Renard P, Ottowitz D, Schiller A, Supper R, Cornaton F (2013) A method for the stochastic modeling of karstic systems accounting for geophysical data: an example of application in the region of Tulum, Yucatan Peninsula (Mexico). *Hydrogeol J* 21(3):529–544. <https://doi.org/10.1007/s10040-012-0944-1>
- Weidie AE (1985) Geology of Yucatan platform. In: Ward WC, Weidie AE, Back W (eds) *Geology and hydrogeology of the Yucatan and Quaternary geology of northeastern Yucatan Peninsula*. New Orleans Geological Society, New Orleans, LA
- Wilkinson PB, Chambers JE, Lelliott M, Wealthall GP, Ogilvy RD (2008) Extreme sensitivity of crosshole electrical resistivity tomography measurements to geometric errors. *Geophys J Int* 173(1):49–62. <https://doi.org/10.1111/j.1365-246X.2008.03725.x>
- Yang CT, Wang LK (2015) *Advances in water resources engineering*. Springer, Heidelberg, Germany
- Zhou W, Beck BF, Adams AC (2002) Effective electrode array in mapping karst hazards in electrical resistivity tomography. *Environ Geol* 42(8):922–928. <https://doi.org/10.1007/s00254-002-0594-z>
- Zhu J, Currens JC, Dinger JS (2011) Challenges of using electrical resistivity method to locate karst conduits: a field case in the inner Bluegrass region, Kentucky. *J Appl Geophys* 75(3):523–530. <https://doi.org/10.1016/j.jappgeo.2011.08.009>
- Ward WC, Keller G, Stinnesbeck W, Adatte T (1995) Yucatán subsurface stratigraphy: implications and constraints for the Chicxulub impact. *Geology* 23(10):873–876. [https://doi.org/10.1130/0091-7613\(1995\)023<0873:YNSSIA>2.3.CO;2](https://doi.org/10.1130/0091-7613(1995)023<0873:YNSSIA>2.3.CO;2)